The Definition of GOES Infrared Lightning Initiation Interest Fields

RYAN J. HARRIS

Department of Meteorology and Space Systems Academic Group, Graduate School of Engineering and Applied Sciences, Naval Postgraduate School, Monterey, California

JOHN R. MECIKALSKI

Atmospheric Science Department, University of Alabama in Huntsville, Huntsville, Alabama

WAYNE M. MACKENZIE JR.

Earth Systems Science Center, National Space Science and Technology Center, University of Alabama in Huntsville, Huntsville, Alabama

PHILIP A. DURKEE AND KURT E. NIELSEN

Department of Meteorology and Space Systems Academic Group, Graduate School of Engineering and Applied Sciences, Naval Postgraduate School, Monterey, California

ABSTRACT

Within cumulus cloud fields that develop in conditionally unstable air masses, only a fraction of the cumuli may eventually develop into deep convection. Identifying which of these convective clouds is most likely to generate lightning often starts with little more than a qualitative visual satellite analysis. The goal of this study is to identify the observed satellite infrared (IR) signatures associated with growing cumulus clouds prior to the first lightning strike, or lightning initiation (LI). This study quantifies the behavior of 10 *Geostationary Operational Environmental Satellite-12* (*GOES-12*) IR fields of interest in the 1 h in advance of LI. A total of 172 lightning-producing storms, which occurred during the 2009 convective season, are manually tracked and studied over four regions: northern Alabama, central Oklahoma, the Kennedy Space Center, and Washington, D.C. Four-dimensional and cloud-to-ground lightning array data provide a total cloud lightning picture (in-cloud, cloud-to-cloud, cloud-to-air, and cloud-to-ground) and thus precise LI points for each storm in both time and space. Statistical significance tests are conducted on observed trends for each of the 10 LI fields to determine the unique information each field provides in terms of behavior prior to LI. Eight out of 10 LI fields exhibited useful information at least 15 min in advance of LI, with 35 min being the average. Statistical tests on these eight fields are compared for separate large geographical areas. Median IR temperatures and 3.9-μm reflectance values are then determined for all 172 events as an outcome, which may be valuable when implementing a LI prediction algorithm into real-time satellite-based systems.

1. Introduction

Lightning is one of Earth's most awe-inspiring atmospheric phenomena, yet our knowledge of exactly how and when it will occur remains an elusive research problem today. The main goals of this study are to understand the behavior of infrared (IR) and visible (VIS) imagery of geostationary satellite-sensed cloud-top properties as cumulonimbus (Cb) clouds begin to form an initial lightning flash, so-called lightning initiation (LI), using statistical analysis to identify valuable satellite-derived interest fields (IF) and suggest preliminary "critical" or median values per field.

Cloud-to-ground (CG) lightning is one of the primary types of cloud-borne electrical discharge. While CG strikes make up a minority of total lightning, they significantly impact human populations. Over the 10-yr period 1999–2008, lightning caused an average of 43 direct fatalities, 266

Corresponding author address: John R. Mecikalski, Atmospheric Science Department, University of Alabama in Huntsville, National Space Science and Technology Center, 320 Sparkman Drive, Huntsville, AL 35805-1912.
E-mail: johnm@nsstc.uah.edu

injuries, and more than $47.2 million in property, forest, and crop damage per year across the United States and its territories (National Weather Service 2010). Curran et al. (2000) cited additional insurance reports that suggest the annual cost of lightning damage in the United States could be closer to $1 billion. Lightning also killed more people per year than tornadoes and hurricanes, and was second only to floods during the 30 years leading up to 1994 (Curran et al. 2000). CG strikes also indirectly impact people via lightning-induced fires and power outages, and is particularly disruptive to airport operations and many activities that require people to be outdoors immediately before, during, and after thunderstorms.

The prediction of lightning within a storm has been done using radar data (Keighton et al. 1991; Hondl and Eilts 1994; Gremillion and Orville 1999), and only recently with other techniques (Mazany et al. 2002; Short et al. 2004). Satellite and lightning data have been combined to estimate storm severity from cloud-to-ground flash rates (Goodman et al. 1988; Roohr and Vonder Haar 1994), where it was *suggested* that the prediction of lightning may be possible using IR imagery, and would be valuable to forecasters of severe weather, aviation hazards, or forest fires. Previous satellite and lightning research has focused primarily on identifying precursors to severe thunderstorms after lightning has already begun. In contrast, this study evaluates the effectiveness of specified Geostationary Operational Environmental Satellite (GOES) IR, so-called interest fields, in *forecasting the onset of lightning* in the 1-hr time period (so-called nowcasting) following initial satellite detection of a growing cumulus cloud.

Knowledge of the beginning of the Bergeron process within growing convective clouds serves as a proxy for noninductive charging (Reynolds et al. 1957). Inferring the occurrence of noninductive charging within satellite-observed clouds is challenging, requiring that sound relationships be formed between cloud-top IR signatures and in-cloud (IC) processes related to glaciation and ice mass flux (Cecil et al. 2005; McCaul et al. 2009). From current geostationary satellite imagery over the United States, the former can be gleaned from 3.9-μm reflectivity (as a proxy for cloud-top glaciation), while the latter can be obtained from inferred updraft strength information such as cloud-top cooling rates (Roberts and Rutledge 2003) and other IR-based fields (Mecikalski and Bedka 2006, hereafter MB06; Mecikalski et al. 2010a,b). Thus, the potential exists to estimate LI for rapidly growing convective clouds within a convective initiation (CI) nowcasting algorithm such as the Satellite Convection Analysis and Tracking (SATCAST; MB06) system, or the AutoNowcaster (Mueller et al. 2003).

Section 2 of this paper provides background on the thunderstorm electrification process, as well as noninductive charging, for which geostationary satellite data fields can serve as proxy indicators of its occurrence. Section 3 describes the data used, while section 4 presents the processing methodology. The study's main results and conclusions are presented in sections 5 and 6, respectively.

2. Background

a. Thunderstorm electrification

The electrification process itself is complex and still poorly understood largely because of the difficulty observing the phenomenon in nature. Lightning discharge processes span 15 orders of magnitude in scale, from atomic-scale electron transfer to thunderstorm dynamics tens or hundreds of kilometers in size (Williams 1988). The reader is directed to other well-documented literature for a more in-depth discussion (Krehbiel 1986; Williams 1988; Saunders 1993).

Many dynamical and microphysical processes occur to yield lightning before a strong vertically developing cumulonimbus cloud top reaches the tropopause. Initially, a nascent Cb contains only liquid cloud droplets. Precipitation processes usually begin as a cumulus cloud top lifts through the 0°C level, driven vertically by the updraft (Bergeron 1935; Houghton 1950; Dye et al. 1974). Cumulus cloud droplets remain supercooled liquid until the cloud ascends to temperatures of around −15°C where freezing (glaciation) begins to occur, resulting in the so-called mixed-phase region of a cloud. As the Cb grows, a reservoir of supercooled droplets forms between −5° and −15°C. Cloud droplets freeze into ice crystals, graupel, or hail as the Cb continues to ascend through the −15° to −20°C level. Graupel forms when supercooled droplets freeze on contact with other ice particles. Gravity then separates the heavier ice particles from lighter ice particles within the updraft. The heavier particles settle or fall through the supercooled droplets in the mixed-phase region where the primary storm electrification is thought to occur.

It is widely believed that collisions of supercooled droplets and ice particles under prevailing vapor and air pressures and temperatures of the mixed-phase region prompt transfers of electrical charge (Reynolds et al. 1957; Dye et al. 1989). Collision events are most numerous in a cloud's updraft and mixed-phase regions, and are proportional to updraft strength. The positive charges generally transfer to lighter cloud particles and are carried aloft by the updraft into the upper region of a Cb. Meanwhile, the heavier particles that remain in the mixed-phase region take on a negative charge. The negative charge accumulating in the mixed-phase region induces a positive charge at and near Earth's surface. The electric field, or

TABLE 1. Convective initiation and lightning initiation interest fields and their respective thresholds used in MB06, Siewert (2008) and what this study considers. The last column summarizes each field's physical description.

Interest field	MB06 critical CI value	Siewert LI value	15–30-min threshold (this LI study)	Description
10.7-μm T_B	<0°C	≤−13°C	<0°C	Cloud tops cold enough to support supercooled water and ice mass growth; cloud-top glaciation
10.7-μm T_B time trends[a]	<−4°C (15 min)$^{-1}$ [ΔT_B (30 min)$^{-1}$ < ΔT_B (15 min)$^{-1}$]	≤−10°C (15 min)$^{-1}$	<−6°C (15 min)$^{-1}$	Cloud growth rate (vertical)
Timing of 10.7-μm T_B drop below 0°C	Within prior 30 min	Not used	Not used	Cloud-top glaciation
6.5–10.7-μm T_B difference	T_B diff: −35°C to −10°C	≥−17°C	>−30°C	Cloud-top height relative to mid/upper troposphere
13.3–10.7-μm T_B difference	T_B diff: −25°C to −5°C	≥−7°C	>−13°C	Cloud-top height relative to mid/upper troposphere; better indicator of early cumulus development but sensitive to cirrus
6.5–10.7-μm T_B time trend	>3°C (15 min)$^{-1}$	≥5°C (15 min)$^{-1}$	>5°C (15 min)$^{-1}$	Cloud growth rate (vertical) toward dry air aloft
13.3–10.7-μm T_B time trend	>3°C (15 min)$^{-1}$	≥5°C (15 min)$^{-1}$	>4°C (15 min)$^{-1}$	Cloud growth rate (vertical) toward dry air aloft
3.9–10.7-μm T_B difference[b]	Not used	Not used	>17°C	Cloud-top glaciation
3.9–10.7-μm T_B time trend[c]	Not used	$T − T(t − 1) < −5$°C and $T − T(t + 1) < −5$°C	>1.5°C (15 min)$^{-1}$	Sharp decrease, then increase indicates cloud-top glaciation
3.9-μm fraction reflectance[c]	Not used	≤0.05	<0.11	Cloud top consists of ice (ice is poorer reflector than water at 3.9 μm)
3.9-μm fraction reflectance trend[b]	Not used	Not used	<−0.02 (15 min)$^{-1}$	Cloud-top glaciation rate

[a] Represents two unique 10.7-μm T_B interest fields in MB06. No 30-min trends were used in Siewert (2008) or in this study.
[b] Unique to this study.
[c] Added to MB06 fields by Siewert (2008).

gradient of an electric potential field, increases until the insulating properties of the air break down. The resultant lightning discharge briefly neutralizes the electric field.

b. Nowcasting CI and LI using geostationary satellite data

Recent studies demonstrate that IR satellite imagery can provide quantitative assessments of cumulus cloud growth leading to CI (MB06) and LI (Siewert 2008). Roberts and Rutledge (2003) and MB06 define CI as the first occurrence of a precipitation echo with ≥35-dBZ intensity in the lowest radar scan level from a convective cloud. MB06 defined the behavior of 8 GOES IR IFs and defines IR blackbody brightness temperature (T_B) thresholds per IF as precursors to CI. The CI IFs are based on channel difference and time trends using three of the four GOES IR channels (not 3.9-μm). Mecikalski et al. (2008) evaluated the usefulness of a CI nowcasting tool using the MB06 results. Siewert et al. (2010) applied a similar methodology to the Meteosat Second Generation (MSG) satellite data in Europe, modeled after Mecikalski et al. (2010a).

Setvák and Doswell (1991), Lindsey et al. (2006), and Rosenfeld et al. (2008) identified microphysical characteristics of growing convective clouds using the GOES and MSG 3.9-μm imagery. These recent advances are important for providing microphysical clues to lightning generation given the water versus ice sensitivity of the 3.9-μm channel; the 3.9-μm channel can be used to indicate whether cloud-top glaciation is occurring, or specifically the transition of supercooled cloud droplets to ice crystals. Siewert (2008) initially demonstrated the usefulness of the GOES 3.9-μm and other IR channels in nowcasting LI using a small database of 12 events (for which this study extends). Table 1 summarizes the CI and LI IFs that MB06 and Siewert (2008) employed, also listing additional fields this study explores.

Thunderstorm diagnostic research using geostationary satellites has often focused on linking thunderstorm intensity with time changes observed in imagery. Adler and Fenn (1979) and Rosenfeld et al. (2008) studied the vertical growth rate of severe and tornadic convection using IR imagery. Adler and Fenn (1979) derived vertical

velocity and divergence fields associated with active storms, while Adler and Mack (1986) examined Cb anvil characteristics and flows. Rosenfeld et al. (2008) correlated hail and tornadoes in thunderstorms to diagnose effective cloud-top particle radius fields, relying on the 3.9-μm channel. Goodman et al. (1988) and Roohr and Vonder Haar (1994) utilized geostationary imagery and lightning data to demonstrate general convective patterns.

With lightning detection being a burgeoning field in remote sensing, storms that have already initiated lightning are central to such research. Focus has shifted from solely CG lightning studies to total cloud lightning (TCL) examination (i.e., combined CG and IC lightning) in the past decade. Goodman et al. (2005) and MacGorman et al. (2008) used TCL to infer storm severity. Additionally, McCaul et al. (2009) showed how TCL can help nudge mesoscale model resolution of microphysical processes related to lightning.

This study is guided by the following hypotheses: 1) LI nowcasting from GOES is a viable capability, which can be improved with a better understanding of how to use and interpret quantified GOES data; and 2) the 3.9-μm channel is underutilized in LI nowcasting and can provide information on cloud-top glaciation with significant forecast value. Overall, the primary goal of this work is to identify which field or combination of fields provides the most accurate and timely (predictive) indication of imminent lightning production in convective storms.

3. Data

Five channels on the *GOES-12* imager retrieve radiance reflected or emitted by Earth in various wavelength bands. The VIS channel senses reflected radiance centered on 0.65 μm. Channels 2, 3, 4, and 6 retrieve terrestrially emitted radiance. The 3.9-μm channel is unique in that it senses reflected solar radiance, as well as emitted IR energy, or emittance. The 3.9-μm channel encounters very little attenuation or absorption by atmospheric gases or aerosols and is highly sensitive to water versus ice hydrometeors. The 6.5-μm channel is sensitive to water vapor, the 10.7-μm channel is known as the "clean window" since it experiences very little atmospheric attenuation, and the *GOES-12* 13.3-μm channel includes emission from carbon dioxide. All IR channels are 4-km resolution except the 13.3-μm channel, which is 8-km resolution (Menzel and Purdom 1994).

Remotely sensing TCL began as the first Lightning Detection and Ranging (LDAR) system was installed at Kennedy Space Center (KSC), Florida, in the 1970s. Since then, the Lightning Mapping Array (LMA) was born out of lightning research at New Mexico Tech (Krehbiel et al. 2000; Thomas et al. 2001). The LMA locates lightning

radiation sources in three spatial dimensions and time. The array is a mesoscale network of Global Positioning System Time-of-Arrival (GPS-TOA) sensors that detect very high frequency (VHF) signals at unused television frequencies. The arrays are $\sim$(60 $\times$ 80) km in size. For this study, we used the four-dimensional (4D) TCL data from three of the four existing LMAs. The Central Oklahoma LMA (OKLMA) and the North Alabama LMA (NALMA) consist of 11 and 13 GPS VHF receivers, respectively, which sense lightning source radiation in the 54–88-MHz range. The Washington, D.C., LMA (DCLMA) is the newest operational LMA, and it contains 10 sensors that detect lightning sources in the 192–198-MHz radio frequency range. The higher VHF channel is used in the DCLMA to limit the effects of increased radio frequency noise in an urban environment (Krehbiel et al. 2006). The LMA's flash detection efficiency approaches 100% within the 60 $\times$ 80-km array and decreases outward. The location accuracy degrades quadratically with distance from the center (Koshak et al. 2004; Thomas et al. 2004). The NALMA, as noted by Goodman et al. (2005), is nominally accurate to within 50 m inside the 150-km array center.

This study used preprocessed "decimated" LMA data. While decimated data are not as detailed as fully postprocessed data, they are sufficiently detailed for most uses (Rison et al. 2003). From these data, the following information was used for each source detected by the array: decimal time, latitude, longitude, and altitude.

The 4D Lightning Surveillance System (4DLSS), which replaced the legacy LDAR system, has both a CG and TCL sensor array. Like the LMA, the 4DLSS's TCL array uses VHF and TOA techniques to pinpoint lightning sources. The array consists of nine 60–66-MHz VHF sensors spread across an estimated 45 $\times$ 65 km^2 area that includes the KSC complex. The flash detection efficiency is 100% within the array and 90% at 111 km from the array center. Like the LMA, the location accuracy degrades quadratically with distance from the center. The location error is <2 km at 111 km from the center (Murphy et al. 2008). The 4DLSS is slightly less accurate than the LMA at distances beyond its 45 $\times$ 65 km^2 network since the 4DLSS array area is smaller. 4DLSS data were obtained from the National Aeronautics and Space Administration (NASA) (NASA 2010). The Cloud-to-Ground Lightning Surveillance System that is part of the 4DLSS was not used in this study.

4. Processing methodology

As a means of meeting this study's objectives and addressing the research hypotheses, the following analysis procedures are developed. This study considers summertime convection that occurred between 24 May
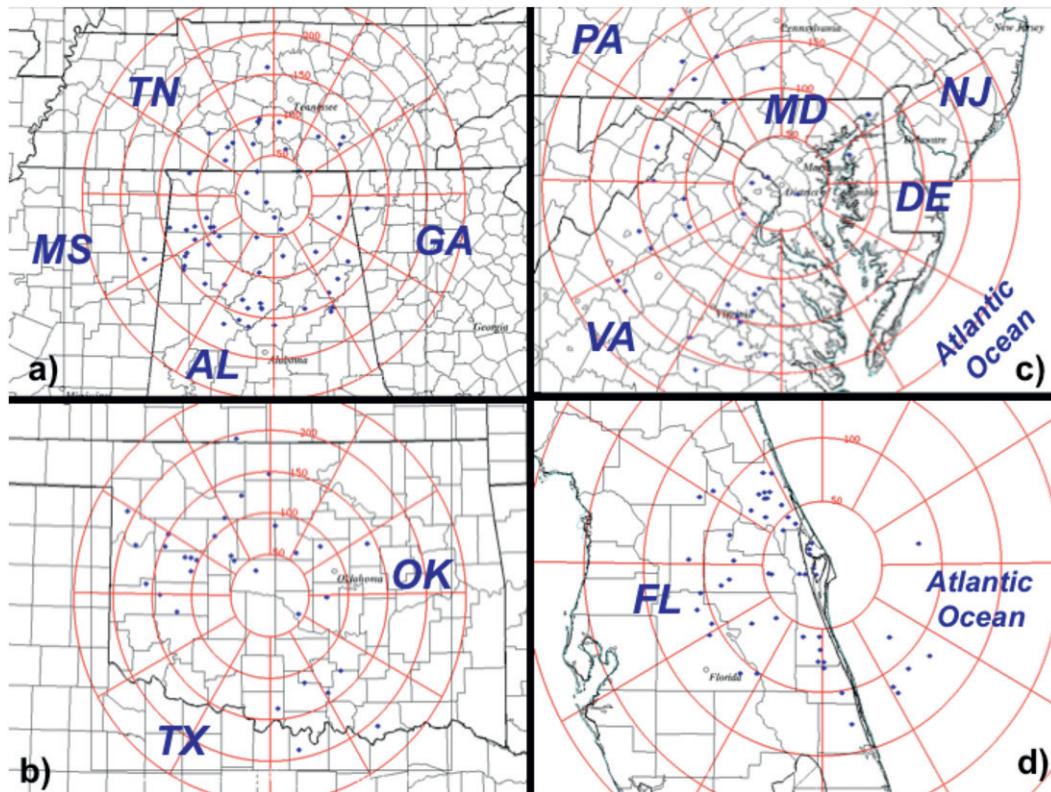
FIG. 1. The 4D lightning arrays used in this study. The 172 LI storm cases are denoted as blue dots. (a) The NALMA 11 sensors near Huntsville, AL and 2 sensors near Atlanta, GA. (b) The OKLMA 11 sensors south and west of Oklahoma City, OK. (c) The DCLMA 10 sensors around Washington, DC. (d) The 4DLSS 9 sensors around Cape Canaveral, FL. Range rings are spaced every 50 km. The center points for each array are as follows: NALMA, OKLMA (35.3365°N, 97.7474°W), DCLMA (38.9218°N, 77.0208°W), and 4DLSS (28.5385°N, 80.6426°W).

and 23 August 2009, and therefore we expect the results will be most applicable during this time of year.

a. Study region considerations

Before building a storm catalog, the accuracy of each 4D lightning platform is considered to narrow the focus areas. Similar to Goodman et al. (2005), potential storm cases were limited to within 150 km of each LMA array center. Specific LMA detection efficiencies were not available to compare with the 4DLSS; however, since the 4DLSS has a smaller array area, its effective range is smaller. Therefore, the 90% detection efficiency radius (i.e., 100 km) was arbitrarily chosen to restrict the Florida cases in this study, yet a few exceptions were allowed for ideal LI events. Figures 1a–d show the regions of interest.

b. Identifying potential lightning initiators

After the usable radii for each 4D lightning region were determined, *GOES-12* VIS imagery was examined each day for potential LI events by subjectively searching for cumulus fields that later developed into convective storms. Key to the search was newly initiated convection occurring between 1230 and 2359 UTC.[1] Storms with nearby preexisting convection (i.e., within 10 km) were generally excluded from this study because of possible "contamination" from overlying cirrus clouds. Even thin cirrus above developing cumulus clouds will result in colder cloud top T_B values than actually exist, while also altering the microphysical properties estimated from the 3.9-μm channel. Potential storm days for each region were catalogued based on the criteria in Table 2, provided the availability of satellite and lightning data. Once cataloging was complete, *GOES-12* data were collected for all "Excellent" cases. Some "Good" and a few "Fair" cases were used as well, after closer examination revealed less contamination than initially assessed.

c. LMA data

The 4D TCL datasets are extremely voluminous. A single storm can have $O(10^4–10^5)$ individual lightning

---

[1] Local time is UTC − 6 h for 4DLSS and DCLMA, and UTC − 7 h for NALMA and OKLMA.

TABLE 2. Initial VIS satellite imagery criteria used to identify and catalog potential lightning-initiating convection.

Quality	Inside 100–150-km domain	Preexisting convection	Cirrus contamination
Excellent	Yes	No	No
Good	Yes	Minimal	Minimal
Fair	No	Likely	Likely

TABLE 3. Clustering thresholds for each 4D lightning flash-grouping algorithm including the original LDAR, the new 4DLSS, and the LMA. (ND = Not defined/used.)

Criteria	Flash-grouping algorithm thresholds		
	LDAR[a]	4DLSS[b]	LMA[c]
Max flash time (s)	3	3	ND
Max time between sources (s)	0.5	0.3	0.3
Max time between branches (s)	0.03	0.03	ND
Max flash coverage (km)	5	1	1
Max allowable angle error (°)	1	2.9	2.9
Additional criteria	ND	ND	Various[c]

[a] Nelson (2002).
[b] Matched McCaul et al. (2009) for consistency in this study.
[c] McCaul et al. (2009).

radiation source events, and single flashes can contain anywhere from a few to >1000 sources. Many of the potential storm days had ≥1 million source events. Thousands of source events can occur in only 1–2 s. Recall, the goal was to identify when LI occurred (i.e., the first source in a Cb). To reduce data volume while ensuring event (flash) detection, the 4D data were processed using two flash-grouping algorithms, similar to the National Lightning Detection Network (NLDN; Orville 1991; Orville and Huffines 2001) flash-grouping algorithm. One algorithm processed 4D lightning data for the three LMAs, and the second algorithm grouped lightning sources into probable flashes for the 4DLSS. Also tracked were first-time CG occurrences using NLDN data in order to verify the 4D flash-grouping results, and additionally to measure the time lag from first-time IC to CG lightning.

The LMA flash-grouping algorithm for this research was supplied by the National Space Science Technology Center at the University of Alabama in Huntsville (McCaul et al. 2009). The algorithm employs time and space proximity criteria to identify the sources belonging to a given flash. Sources are assumed to belong to the same flash if they occur less than 0.3 s apart in time and also satisfy a spatial separation requirement.

Sources were assigned a flash number, followed by the filtering of what McCaul et al. (2009) termed "singletons." A flash containing only one source is considered to be either erroneous or atmospheric VHF noise. Therefore, flashes with 2–10+ sources define an accurate flash measurement. This study assumes that a flash contains at least 4 sources. After filtering, the first source within the flash is defined to be the originating source. Subsequently, flash-grouped LMA files were created for each potential storm day containing flash time and location (latitude, longitude, and altitude) represented by the parent source of each flash.

d. 4DLSS data

Because of 4DLSS data format differences, a different flash-grouping algorithm was needed. McNamara (2002) and Nelson (2002) used a flash-grouping algorithm to cluster lightning sources for the original LDAR sensor. This study used the flash-grouping algorithm from Nelson and the new 4DLSS accuracy numbers identified by

Murphy et al. (2008) to cluster lightning sources into probable flashes. Finally, for consistency, the 4DLSS clustering thresholds were changed to more closely match those used in the LMA algorithm. Table 3 shows the original LDAR flash-grouping algorithm's clustering thresholds alongside the new 4DLSS flash-grouping algorithm, as well as the LMA thresholds for comparison.

As with the LMA data, a valid flash contained at least 4 sources; all flashes with <4 sources were removed. Latitude–longitude–altitude coordinates and the geodetic approximation calculations that take Earth's curvature into consideration were used (McNish 2010). Subsequently, flash-grouped 4DLSS files were created for each storm day, also listing each flash by time and location represented by the parent source of each flash.

e. Identifying individual storm cases

Once the lightning and satellite data were prepared, individual storm cases were identified. For each day with active lightning, individual cells were studied from the precumulus stage to LI. (Convective cells that failed to produce lightning were generally ignored for this study.) The sample storm set was limited to a specific time window each day as the 3.9-μm reflectance (ref39) becomes undefined as the solar zenith angle approaches 90° (i.e., sun on horizon). Specifically, Lindsey et al. (2006) determined the GOES ref39 to be most usable when the solar zenith angle is ≤68°. Individual storm cases were selected within the following approximate time windows based on Lindsey et al. (2006)'s 68° rule: NALMA (1305–2230 UTC), 4DLSS (1242–2208 UTC), OKLMA (1351–2315 UTC), and DCLMA (1230–2152 UTC). Both the 1-min grouped NLDN CG and 4D IC data were overlaid on top of the satellite images. The NLDN observes a small percentage of IC flashes while the 4D lightning array can observe CG flashes.

Once potential lightning-initiating convection was located, the analysis began one satellite image time step prior to the first sign of a cumulus cloud field, and at least one hour prior to the earliest of the following: the storm's first lightning occurrence, or the storm's 10.7-μm T_B decrease to 253 K. Krehbiel (1986) referenced the $-20°$C level as the point at which storms become strongly electrified. Each storm's analysis was ended 30 min after the earliest occurrence of the following: final lightning flash, the storm's 10.7-μm T_B reaching 253 K, or after rapid storm dissipation.

Similar to Siewert (2008), the storm centroid was identified as the coldest 10.7-μm T_B, which typically indicates the region of strongest storm updraft. In a Lagrangian frame, a storm's coldest 10.7-μm T_B was tracked throughout each case's lifetime. Strong vertical wind shear complicates cloud-top T_B measurements, as the stronger winds aloft displace the coldest 10.7-μm T_B pixel downstream of the main updraft. Therefore, the number of strong vertical wind shear cases was limited.

f. Collecting storm measurements

After the appropriate time window was established for each case, pre- and post-LI environmental measurements were collected from 1 h before to ½ hour after LI. The following *GOES-12* IR parameters were analyzed: 3.9-μm T_B (T_{B39}), 3.9-μm radiance (39rad), 6.5-μm T_B (T_{B65}), 10.7-μm T_B (T_{B107}), and 13.3-μm T_B (T_{B133}). The T_B's were recorded to the nearest 0.1 K, and the radiances were recorded to the nearest 0.001 W m^{-2} str^{-1} (str = steradian). Finally, the LI time was identified as the first IC or CG flash to the nearest minute. Figure 2 illustrates the tracking done with respect to one LI event.

g. GOES LI interest fields

1) INTEREST FIELD SELECTION

Previous CI–LI work as outlined above provided a solid foundation for this study. The same 8 GOES LI IFs used in Siewert (2008) were explored, and two additional fields were added (see Table 1): T_{B107}, 15-min T_{B107} trend, 6.5–10.7-μm difference (T_{B65107}), 13.3–10.7-μm difference ($T_{B133107}$), 15-min T_{B65107} trend, 15-min $T_{B133107}$ trend, 3.9–10.7-μm difference (T_{B39107}), 15-min T_{B39107} trend, ref39, and 15-min ref39 trend. Since satellite data exhibit disparate time intervals between images (e.g., 5, 10, 13, 17, 31 min), we chose to use a 15-min time tendency for the trend IFs as in MB06 and Siewert (2008).[2] For simplicity, linear storm growth was assumed between successive

---

[2] Note, the 30-min 10.7-μm cloud-top T_B trend was used in MB06, as in Roberts and Rutledge (2003), yet not in Siewert (2008) or in this study. This was done to minimize cloud tracking-induced errors caused by using only two images 15 min apart in time.
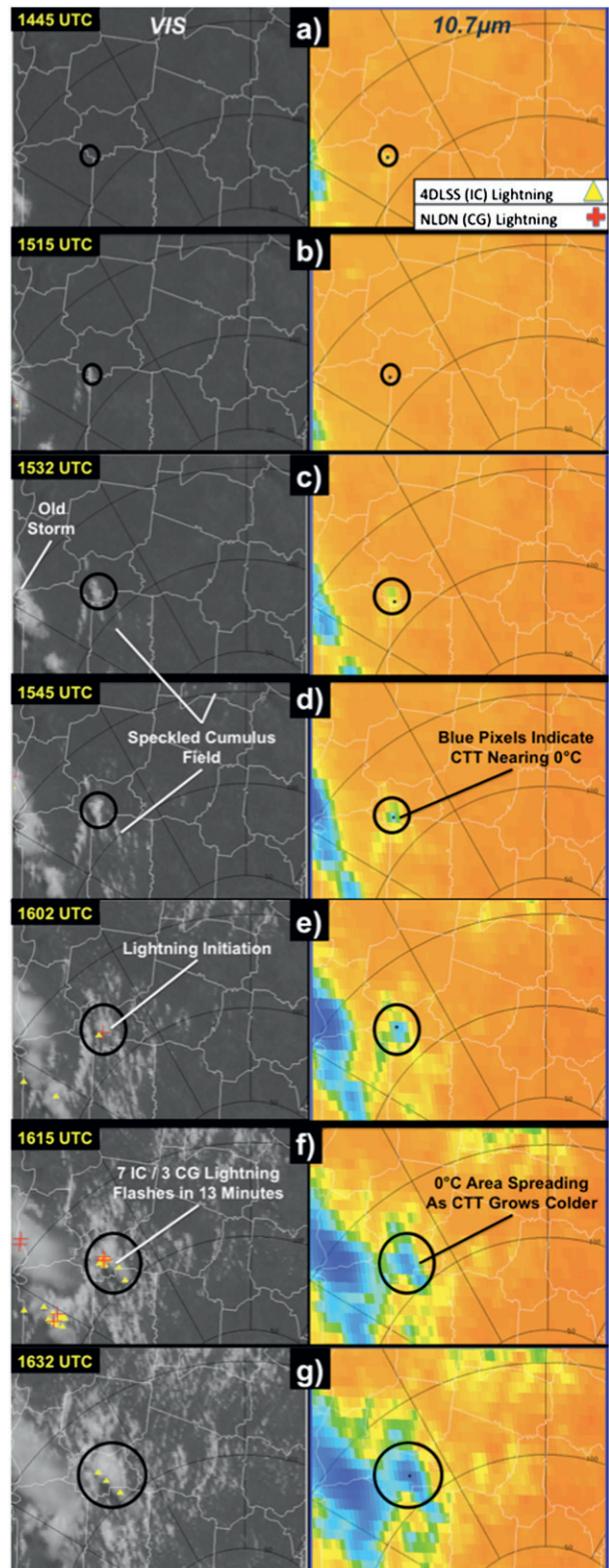
FIG. 2. Example of storm tracking from (a) 1 h before LI 1445 UTC to (g) 30 min after LI 1632 UTC. Pictured are *GOES-12* VIS at left and 10.7-μm imagery at right with lightning also depicted.

satellite images (even though deep convection often exhibits highly nonlinear atmospheric tendencies). The 3.9-, 6.5-, and 13.3-μm channels were not included as standalone IFs, as other studies relating these fields to cloud properties determined that the aforementioned channels show little to no significant "stand alone" signal leading up to LI (MB06; Siewert 2008).

2) 3.9-μm REFLECTANCE

Previous research demonstrated the ref39's usefulness, particularly with regard to water-versus-ice delineation in convective clouds (Setvák and Doswell 1991; Lindsey et al. 2006). The total 3.9-μm radiance received at the satellite, $R_{3.9\mu m}$, is described as

$$R_{3.9\mu m} = \text{ref39} + e_{3.9\mu m} R_{\text{emit39}\mu m}(T), \quad (1)$$

where the second term is the product of an object's 3.9-μm emittance and its emissivity, $e_{3.9\mu m}$. The sensed objects (cloud mass) are assumed to be perfect blackbodies at 3.9 μm, and thus $e_{3.9\mu m} + \text{ref39} = 1$, for clouds of sufficient optical thickness. Obtaining ref39 from Eq. (1) follows the methodology of Setvák and Doswell (1991) and Lindsey et al. (2006).

The total amount of Earth-absorbed solar radiance at 3.9 μm, assuming the Sun's blackbody temperature is 5800 K and using the *GOES-12* Planck function constants and solar radiance equation, is given by

$$R_{\text{emit3.9}\mu m}(T_{\text{sun}}) = \frac{\text{fk1}_{3.9\mu m}}{\exp\left[\dfrac{\text{fk2}_{3.9\mu m}}{\text{bc1}_{3.9\mu m} + (\text{bc2}_{3.9\mu m} T_{\text{sun}})}\right] - 1}, \quad (2)$$

where fk1, fk2, bc1, and bc2 are all 3.9-μm GOES-specific constants (CIMSS/SSEC 2010). Next, the 3.9-μm solar flux at the top of the atmosphere is given by

$$S_{3.9\mu m}(r, \xi) = [R_{\text{emit3.9}\mu m}(T_{\text{sun}})](R_{\text{sun}}/r_E)^2 \cos\xi, \quad (3)$$

where R_{sun} is the sun's radius (6.96×10^8 km), r_E is Earth's orbit radius (1.496×10^{11} km), and $\cos\xi$ uses the solar zenith angle (ξ).

With the solar flux calculated, the 3.9-μm emitted Planck blackbody radiance is estimated, as noted from Kidder and Vonder Haar (1995), by

$$B_{3.9\mu m}(T_{B107}) = \frac{c_1 \lambda^{-5}}{\exp\left(\dfrac{c_2}{\lambda T_{B107}}\right) - 1}, \quad (4)$$

where $c_1 = 1.19104 \times 10^{-16}$ W m^2 (str)$^{-1}$, $c_2 = 0.014\,387\,69$ m K, and $\lambda = 3.9 \times 10^{-6}$ μm [multiplied by

10^{-6} to obtain the emitted Planck radiance in terms of W m^2 (sr)$^{-1}$ μm^{-1}]. Here, the Planck curve is based on our T_{B107} measurement. The corresponding 3.9-μm point on the Planck curve is the 3.9-μm emittance, assuming the T_{B107} measurement emanated from a perfect blackbody. For optically thick clouds like a deep cumulus, this is a safe assumption (Lindsey et al. 2006). Finally, ref39 is calculated using

$$\text{ref39} = \frac{R_{3.9\mu m} - B_{3.9\mu m}(T_{B107})}{S_{3.9\mu m}(r, \xi) - B_{3.9\mu m}(T_{B107})}. \quad (5)$$

Some minimal error is introduced in assuming only isotropically scattering spherical cloud and precipitation particles (Setvák and Doswell 1991).

3) LIGHTNING INITIATION DATABASE

A database was prepared for temporal and regional comparison analysis, involving the following procedures. First, all storms were oriented to the same temporal plane by converting times to decimal hour. The initial time, whether 1402 or 2231 UTC, for example, is set to 0 min. This standardization allowed for easier comparative storm analysis. Second, the hour period prior to LI is subdivided into 15-min intervals to help estimate the predictive capability of each IF. Quarter-hour intervals were chosen as GOES data are currently available every 15 min on average. In addition, most of the cases developed from the pre-cumulus stage to LI in ≤1 h. The database consisted of IF data at 60 min (LI–60), 45 min (LI–45), 30 min (LI–30) and 15 min before LI (LI–15), and at the LI time (LI–0).

As satellite image intervals and LI-related times consistently did not match in the hour prior to LI, linear interpolation was performed on each IF between satellite data points. Some introduced interpolation error may occur where some IFs exhibit more nonlinear tendencies than others, but is expected to be minor (<5%).

5. Results

Following the methodology above, 172 total LI cases over four geographical regions were analyzed (Fig. 1); at least 30 cases were collected for each region, while two exceptions were made. First, because of a lack of data, five NALMA cases are only partially complete with respect to time. For NALMA LI–60, there are 53/58 cases (i.e., five less than the total), and for LI–45 there are 57/58 cases (i.e., one less than the total). Insignificant degradation to our results is expected given the relatively large sample size. Secondly, 22/172 cases (i.e., 12.8%) occurred outside the 100–150-km array areas. The aforementioned exception was made only if the 4D data appeared to observe the individual storm case well, as defined when a CG flash

occurred within 4.6–6.9 min of an IC flash, depending on the region. The average time between IC and CG flashes in this study—6.9 min for NALMA, 6.8 min for 4DLSS, 4.6 min for DCLMA, and 4.7 min for OKLMA—matched very closely with the approximate 5–10-min interval noted by Williams and Orville (1989) and Williams et al. (2005). Any lightning timing error caused by this exception is determined to be $<(2–3)$ min. Of interest, some storms in three of the regions—13.8% NALMA, 9.8% 4DLSS, and 25.8% OKLMA—exhibited 0 CG flashes within 30 min after the first IC flash.[3]

a. Behavior of individual GOES interest fields

As a means of limiting the presentation, Figs. 3a–g depict the IF results for one LI event in the 4DLSS region (case 39). All 172 cases do not follow the exact behavior of this LI event; however, the qualitative descriptions represent the entire dataset very well.

Figure 3a shows all four GOES IR channels' behavior in the hour before LI. As expected, a gradual T_{B107} decrease is seen between LI–60 and LI–45, with a more precipitous T_{B107} drop especially after LI–30 as the convective cloud grows rapidly into a colder environment. The precipitous T_{B107} drop for some cases, particularly in the 4DLSS region, did not occur until LI–15. Very few cases exhibited only gradual T_B decreases in the 15 min prior to LI, indicating that our dataset contains primarily rapidly developing storms (i.e., reach LI in <1 h; versus slow-building lightning initiators). Also, OKLMA storms showed the most precipitous T_{B107} decreases of all regions, and the drops also occur earlier in the storm's development. One possible reason may be that the OKLMA region possessed higher overall instability compared to the other locations, although we cannot substantiate this claim at this time.

The 15-min T_{B107} trend (Fig. 3b) appears weakly negative (0 to -6 K) for most cases until about LI–30. The trend decreases significantly (>6 K) from LI–15 to LI–30 min as the updraft increases. The OKLMA T_{B107} trends maintain a relatively strong decrease (>6 K) from early in the storm's development leading up to LI, unlike in the other regions, possibly because of more rapidly developing storms (as noted above). Decreases in T_{B107} of >10 K at LI–0 are common for all regions. Compared to other IFs, the T_{B107} trend exhibited moderate variability between cases.

The T_{B65107} and $T_{B133107}$ IFs (Fig. 3c) display similar characteristics. Each of the IFs begins low: T_{B65107} is lower than the $T_{B133107}$ because of the T_{B65} field having a much

colder T_B with respect to the T_{B107} field. Both IFs show steady increases (i.e., becoming less negative) in all four regions, as the convective clouds approach LI. Some T_{B65107} and $T_{B133107}$ values occasionally became neutral near LI–30 before continuing to increase shortly thereafter. Although 4DLSS case 39 does not exhibit this neutral behavior, one potential cause for this temporarily steady behavior may be linked to the convective cloud reaching a capped or stable atmospheric layer and briefly slowing the storm's growth. The T_{B65107} and $T_{B133107}$ difference IFs display very little variability between storms when compared to the other IFs.

Figure 3d shows the T_{B65107} and $T_{B133107}$ 15-min time trend IFs. A weak positive tendency in both IFs occurs during the early storm development stage (<4 K). By LI–30, most storms exhibit a sharper positive trend. The separation between the two IFs occurs as the T_{B65107} trend is larger than the $T_{B133107}$ trend ($>4–6$ K, versus 3–5 K) after LI–45. As the T_{B107} decreases rapidly after LI–30, the gap between it and T_{B65} decreases more quickly than the T_{B107} and T_{B133} curves (Fig. 3a). Like the T_{B65107} and $T_{B133107}$ IFs, their respective trends show little variability between storms when compared to the other IFs.

The T_{B39107} difference IF (Fig. 3e) typically had a steady or perhaps a slight increase in the early storm development stage. The increase is often followed by a sharp decrease, then a further increase about 15–30 min prior to LI, as exhibited by the T_{B39107} curve. The sharp increase was not as apparent for DCLMA, and typically did not occur until the last 15 min before LI. Similarly, the 4DLSS cases showed this increase most often from LI–15 to LI–0. Siewert (2008) suggested the sharp T_{B39107} increase that follows a slight dip or steadiness indicates a rapid increase in ice flux within the storm. Higher ice content decreases the T_{B39}'s reflective component more rapidly than the emitted component, as approximated by T_{B107}. The T_{B39107} difference exhibits the largest variability between storms compared to the other IFs.

The ref39 IF (Fig. 3e) shows little variability between storms when compared with the other IFs. A steady to sharp ref39 decrease is often noticed in the hour before LI. The sharpest drops generally occurred 15–45 min prior to LI. The ref39 occasionally mirrored the slight increase–decreasing trend that the T_{B39107} difference IF exhibits, particularly in the 4DLSS region. Furthermore, nearly all of the 172 storms had ref39 values ≤ 0.05 (5%) from LI–15 to LI–0. Setvák and Doswell (1991) suggest that a Cb has reached complete glaciation at this fraction reflectance threshold. A glaciated cloud infers greater lightning potential since charge separation occurs rapidly with ice crystal and supercooled droplet collisions (Reynolds et al. 1957).

The T_{B39107} and ref39 15-min time trends exhibit characteristics similar to those discussed above. Note the

---

[3] Regional comparisons among the four datasets from the lightning mapping systems will be presented and discussed in a companion paper.
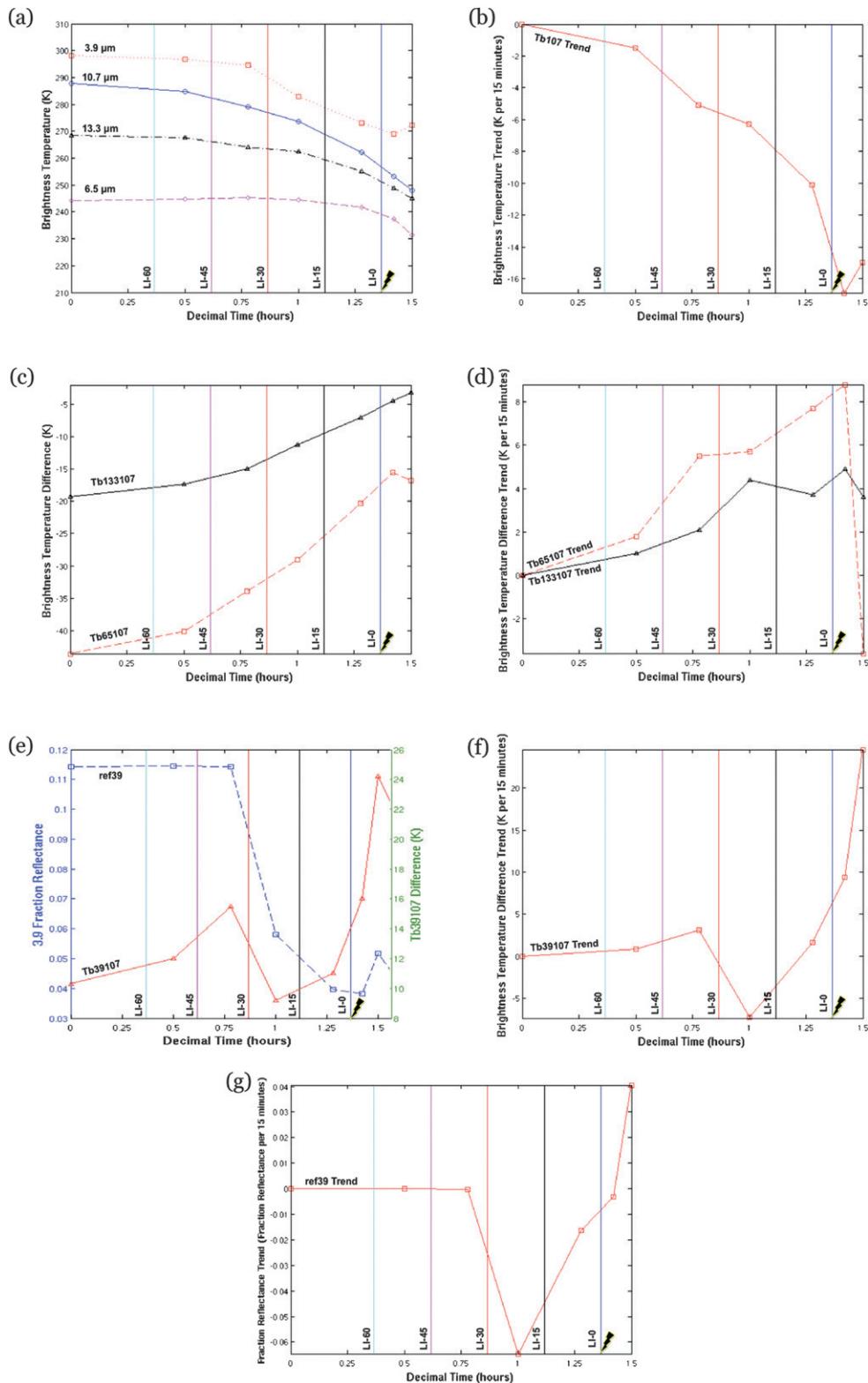
FIG. 3. Behavior of 4 *GOES-12* IR brightness temperatures over time for Florida case 39 in addition to the 9 LI IFs. The vertical LI–0 line represents the first lightning strike, with each vertical line left of LI–0 representing 15-min increments before lightning, up to 60 min before LI (i.e., LI–60). See text for description.
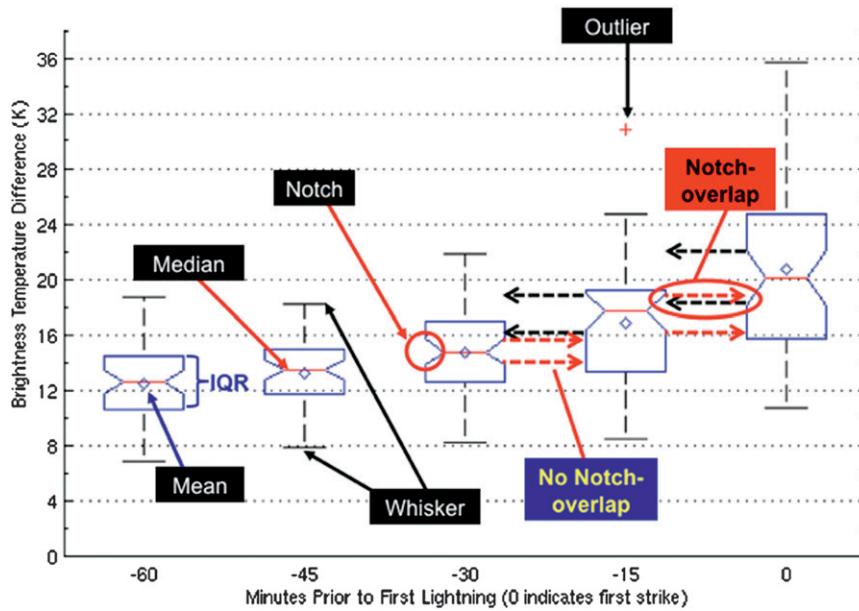
FIG. 4. Box plots description.

weakly positive T_{B39107} trend in Fig. 3f between LI–60 and LI–45, followed by a quick decrease then strong increase by LI–15. Much less T_{B39107} trend variability is seen between storms when compared to T_{B39107}. The 15-min ref39 trend (Fig. 3g) also shows small variability between storms when compared to the other IFs. The ref39 trend generally remains negative throughout the hour leading up to LI and has the most pronounced negative trend 15–45 min before LI.

b. Interest field variability

After each of the 172 cases was qualitatively analyzed, statistics for each of the five LI datasets, from LI–60 to LI–0, were compiled. This was done to show the variability in IFs as a function of time leading up to LI.

For clarity of presentation, box plots (otherwise known as a "box and whisker" plots) are used to qualitatively assess each LI IF's uniqueness per 15-min interval. Figure 4 exemplifies the plotting style used here. Each box plot has a notched box representing the middle 50% of the data, or interquartile range (IQR). A larger IQR indicates higher spread and therefore data variability. The horizontal red line splitting the box in two equal segments (assuming a normal distribution) represents the median (mean values are shown by diamonds). The median and IQR are resistant statistics; whereas outliers adversely impact the mean and standard deviation (Wilks 2006, 26–31). The vertical dashed lines on either side of the IQR (the whiskers) represent ~99% of a distribution from whisker to whisker. Any pluses beyond the whiskers signify outlier data points. The notch within each box plot's IQR represents a visual

statistical significance test. Notch overlap verifies whether each dataset (for a given time) is significantly different than another, and when two-per-time datasets are deemed statistically the same at the $\alpha = 0.05$ significance level. The 5% test level, the most common α threshold, allows one to accept that the notch-overlap hypothesis test may be incorrectly assessing the results ≤5% of the time. If the notches do not overlap (e.g., LI–15 in comparison with LI–30) then the two datasets are deemed significantly different. The width of each notch varies based on each distribution's spread. The main purpose of the notch-overlap test is to determine field uniqueness.

A two-sample t-test hypothesis test was also performed to more thoroughly substantiate the results beyond the visual notch-overlap test. A parametric statistical significance test such as the t test is appropriate since most IFs exhibit a nearly Gaussian distribution. Knowing that the notch-overlap hypothesis test uses the median, the t test was performed using the mean in its hypothesis testing. A two-sample t test assesses whether two sample means are significantly different from each other, assuming the samples are approximately Gaussian. Like the notch-overlap test, the t test was run at the $\alpha = 0.05$ significance level. The null hypothesis is that the means from one distribution time to the next are significantly different. Thus, the alternate hypothesis is that the means are not significantly different (Wilks 2006, 138–145). In other words, the means are the same.

The box plots (Figs. 5a–j) represent the 15-min increment data up to the time of LI. As all four geographical regions showed similar characteristics, the following
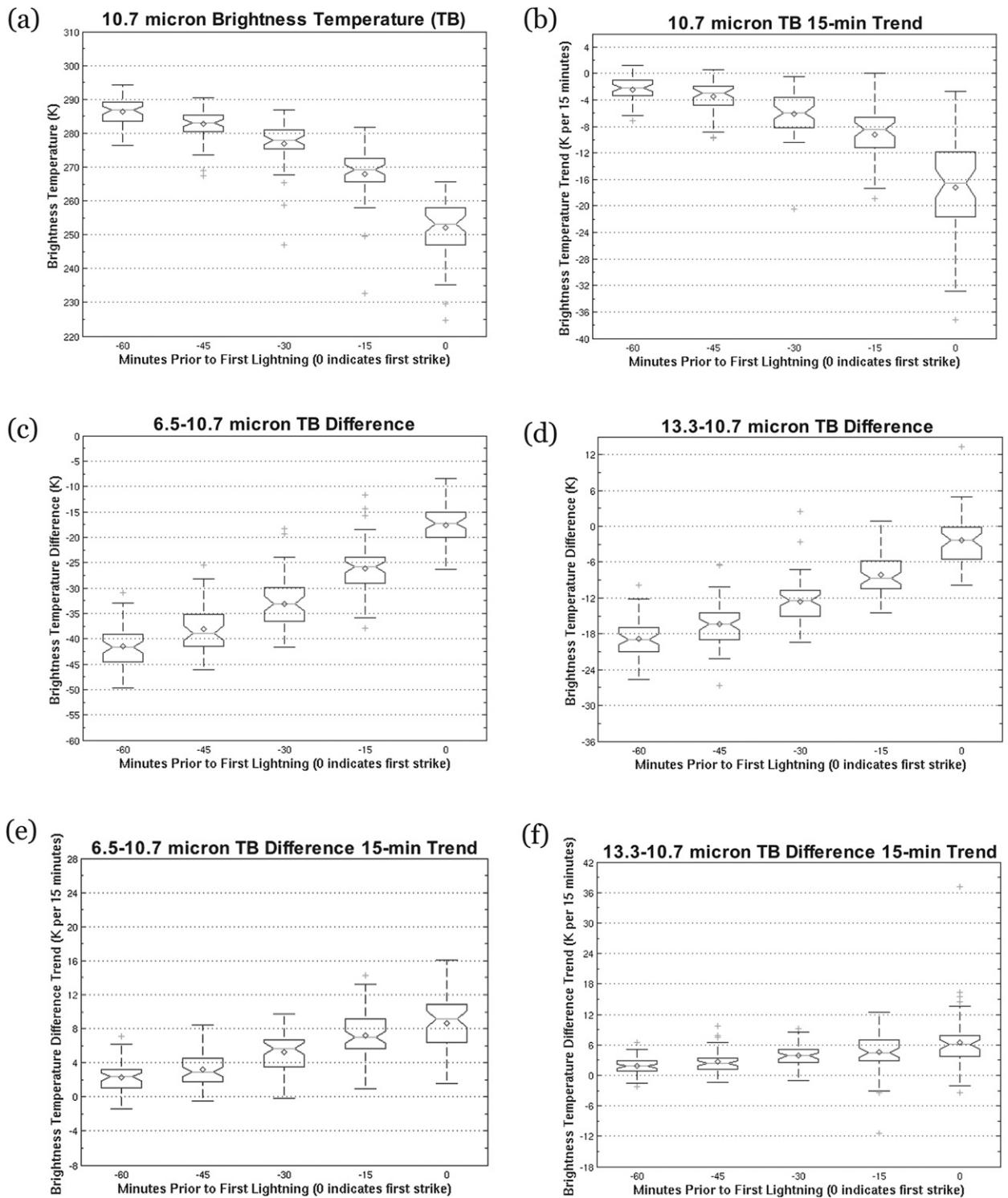
FIG. 5. The LI interest field behavior in the hour prior to LI as represented by 51 Florida cases, using the 4DLSS database. The 0 at the far right represents the 51 cases at the first lightning strike time increment. The box-plot nomenclature is as in Fig. 4.
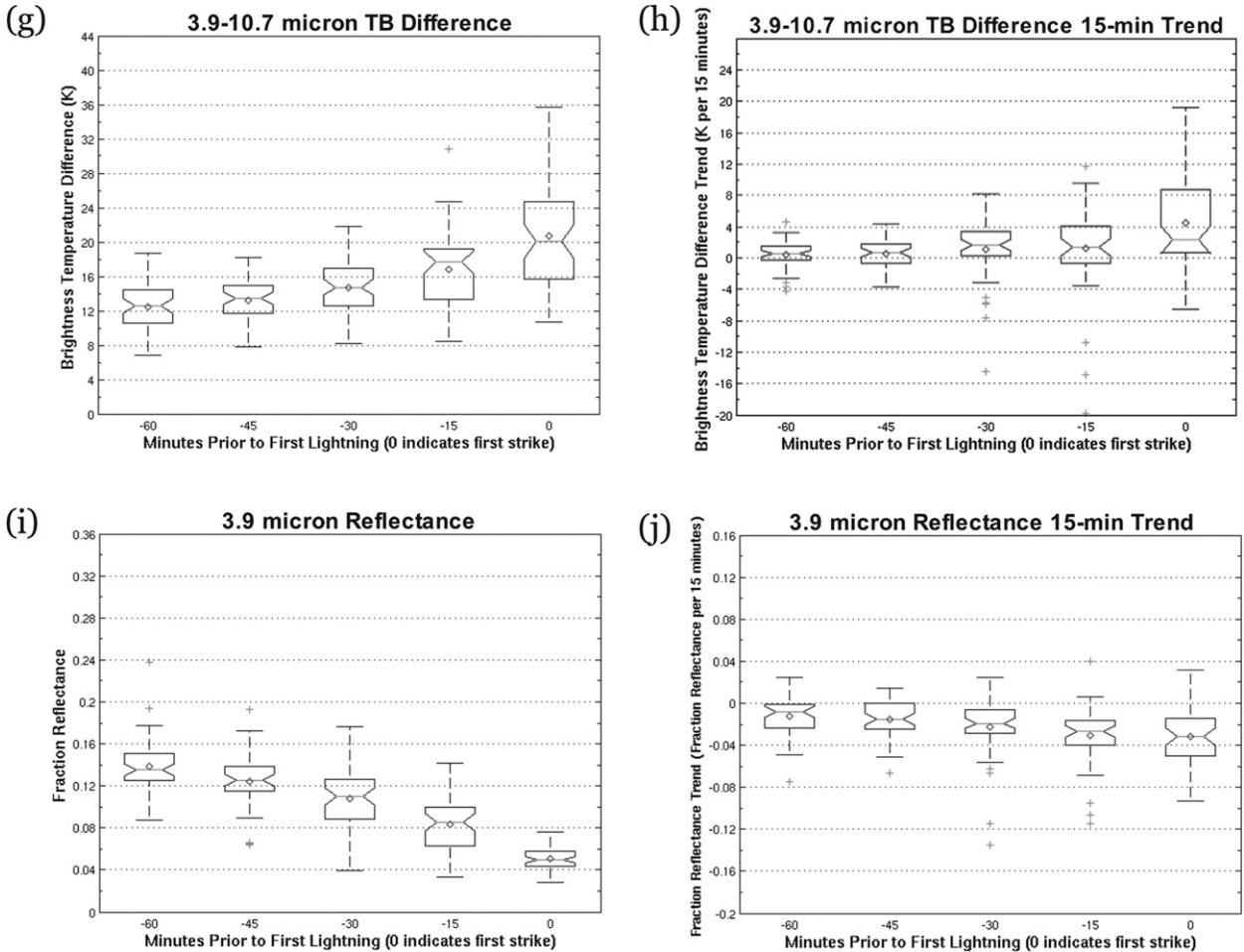
FIG. 5. (*Continued*)

qualitative assessment based on the 4DLSS box plots applies to all regions unless otherwise noted. A few *t*-test results vary from the notch-overlap test since the *t* test is testing against a distribution and its *mean*, while the notch-overlap tests against a distribution and its *median*. Final determination was based on the *t*-test results. Although the *t*-test findings are not shown explicitly, we regularly invoke the results during each IF's notch-overlap discussion.

The pre-LI T_{B107} characteristics for all 51 4DLSS cases (Fig. 5a) closely resemble the behavior of the individual case example shown above. In fact, all IF distributions discussed below match very closely with the one single 4DLSS case explored earlier (Figs. 3a–g). In Fig. 5a, T_{B107} linearly decreases leading up to LI with a distinctly accelerated drop in the last 15–30 min. The notch-overlap test clearly shows no overlap. The T_{B107}'s spread increases by LI–0, which implies a larger degree of variability in cloud microphysics and convective-scale dynamics at LI–0. Like T_{B107}, the pre-LI T_{B107} 15-min time trend is characterized by an accelerating downward

trend, becoming more negative closer to LI. Figure 5b also shows increasing spread from LI–60 to LI–0, indicating a variability pattern similar to the T_{B107} field. Based on the hypothesis test results, the T_{B107} trend field generally exhibits unique behavior in the hour prior to LI.

Figures 5c and 5d show the T_{B65107} and $T_{B133107}$ results, respectively. Each of these IFs clearly increase over time, becoming slightly more accelerated in the last 15–30 min before LI. Here T_{B65107} experiences higher spread compared to $T_{B133107}$, possibly since atmospheric water vapor is influencing the signal at 6.5 μm, which often varies considerably between LI events, and between regions. Both the T_{B65107} and $T_{B133107}$ IFs pass the notch-overlap and *t*-test tests at all times. The pre-LI T_{B65107} 15-min time trend increases linearly (Fig. 5e). The increasing spread with time is attributed to the same cloud microphysics and dynamics that affect the T_{B107} field. Although LI–15/LI–30 and LI–45/LI–60 notch-overlapping is difficult to discern, we deferred to the *t*-test results that indicated T_{B65107} and $T_{B133107}$ uniqueness.

The $T_{B133107}$ 15-min time trend's increase is even subtler than the T_{B65107} trend. Figure 5f also indicates much less spread than the T_{B65107} trend for the same reason discussed above. Less spread reduces potential notch overlap and therefore increases possible uniqueness likelihood; however, Fig. 5f indicates considerable notch overlap, and hence little unique value, because of the subtlety of the $T_{B133107}$ trend's increase. The $T_{B133107}$ trend exhibits relatively redundant information at longer lead times; however, in three of the four regions (i.e., NALMA, OKLMA, and DCLMA) some useful trend information is found at LI–15.

In Fig. 5g, T_{B39107} increases linearly at first and then accelerates 15–30 min before LI. Any notch overlap between LI–0 and LI–15 for 4DLSS is subtle. The accentuated T_{B39107} increase between LI–15 and LI–30 matches the average LI lead time over which T_{B39107} may provide useful information. The T_{B39107} 15-min time trend increases slightly leading up to LI, while the distribution's spread widens (Fig. 5h). The individual trend seen for case 39 is apparent, although is much less for the 4DLSS domain compared to the other regions. The characteristic increase–decrease–increase signal documented by Siewert (2008) is somewhat apparent in the T_{B39107} 15-min time trend distributions; however, this cannot be statistically validated because of marginal notch-overlap and t-test results. Although the up–down–up tendency was noted in individual cases, this tendency is likely washed out when considered within a larger dataset, since this T_{B39107} trend behavior often occurs at different times for each storm from LI–15 to LI–45 min. In addition, the T_{B39107} trend shows little unique information more than 15 min before LI.

As ice content increases volumetrically within a growing storm, ref39 decreases as depicted in Fig. 5i. The decrease is primarily linear and perhaps very slightly accelerated in the last 15–30 min for each region. Regions NALMA, 4DLSS, and DCLMA show complete cloud-top glaciation (i.e., ref39 < 0.05) by LI–0, while over OKLMA, a 0.07 (7%) 3.9-μm fraction reflectance is the average; this small difference is speculated to be a satellite view-angle affect, especially since the OKLMA is farthest west (see Lindsey et al. 2006)[4]. The ref39's notch-overlap and t-test results indicate significant unique information at least 45 min ahead of LI. Although a general decreasing tendency is noted in the ref39 15 min trend (Fig. 5j), the decreases are too subtle. Overall, the ref39 trend provides very little unique information before LI.

---

[4] Lindsey et al. (2006) showed, however, that an increase in cloud base in western U.S. locations leads to lower mixing ratio values for updraft parcels and hence a larger proportion of small particles and increased 3.9-μm reflectance.
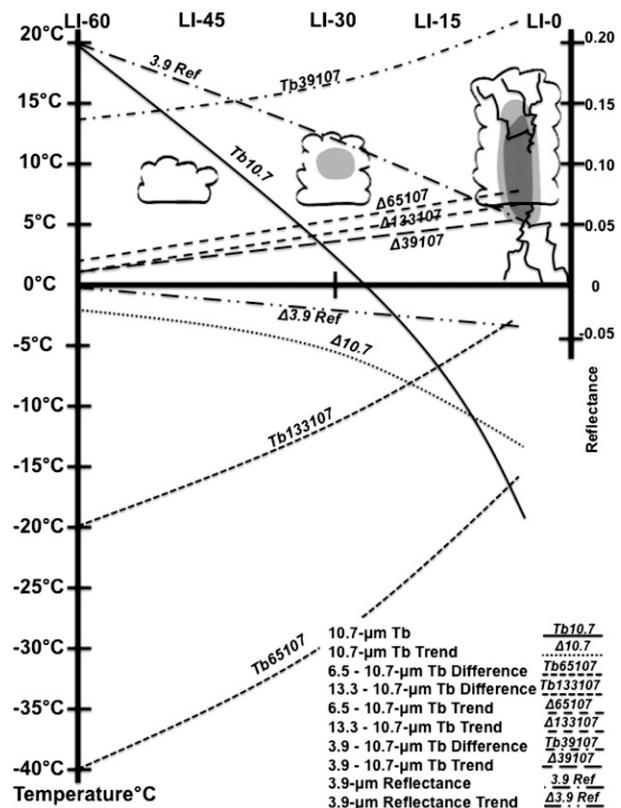
FIG. 6. Conceptual model of LI IF behavior in the hour preceding first lightning, adapted from MB06. Typically, no cloud exists at LI–60. Cumuli begin to appear by LI–4, and precipitation (the gray shading) often forms within the cloud once the cloud-top temperature reaches about 273 K. Lightning initiates at LI–0. The 15-min trend IFs are indicated by Δ.

6. Conclusions

Upon the examination of 172 LI events over the four LMA networks in GOES IR IFs, 8 out of 10 LI IFs considered have at least some unique value in identifying LI across all regions. Statistical significance tests were performed as a means of quantifying IF uniqueness. Table 1 (fourth column) summarizes the findings of Figs. 3a–g, 5a–j, while Fig. 6 presents these results in graphical format. Similar to Siewert (2008), we drew specific IF median values from the results above, as shown in Table 1. These median value LI results are shown along with the MB06 CI thresholds (based on examination of many events, including null CI cases, which was not done here); therefore, the MB06 results can only be qualitatively compared to those found in Siewert (2008) and outward of this study. In Fig. 6, IF values and time trends are depicted for the hour leading up to LI (in a manner similar to Fig. 2 in MB06). These results are applicable for evaluation within a real-time satellite-based system that monitors for LI.

The 15-min T_{B39107} trend and the ref39 trend are the two fields that showed relatively little unique value when GOES IR data were analyzed in advance of LI (hence why 8 of 10 LI IFs are considered valuable). Additionally, the 15-min T_{B65107} and $T_{B133107}$ time trends did not provide much added information. Overall, the 15-min trend IFs provide more awareness to imminent LI. Most fields appear fairly predictive at 15–45 min before LI, with an average lead time for all fields and regions near 35 min.

Given the roughly 35-min average lead time for LI the IFs provide, use of the IF medians and means for LI–15 to LI–30 min determines the values in Table 1. The LI IF values found here are less restrictive than Siewert (2008)'s LI values for two reasons: 1) Siewert (2008) examined convective storms only ≤15 min before LI. Since the LI–0 and LI–15 median values in this study match Siewert's IF values very closely, we feel these two studies corroborate the hypothesis that GOES IR IFs can indeed be used to predict LI. And, 2) this present study makes use of a much larger dataset of LI events (172 versus ~12). With a small database, more extreme values are expected, while smoothing of extreme values occurs as more events are included.

Individual LI cases appear to have very similar tendencies, as for example with the T_{B39107} and $T_{B133107}$ 15-min trends. However, our analysis noted that the largest tendencies often occur at different times in a storm's development, which is likely related to conditions in the ambient environment of a given storm (e.g., instability, the shape of the instability, water vapor profiles). Therefore, use of IFs that appear to provide similar information over a population of events may in fact add valuable information on a case-by-case basis.

Further analysis is required that incorporates an independent dataset containing non-lightning-producing convection so to demonstrate predictability skills (via, e.g., "probability of detection" and "critical success index") before thresholds can be set for use in a real-time LI operational system. The values in Table 1 (fourth column) should be used as general guidance for more empirical, physically based approaches to nowcasting LI using geostationary IR imagery. Before implementation in an LI prediction system, certain inherent difficulties need to be overcome or understood, specifically those associated with preexisting cloudiness (i.e., cirrus, which was avoided in these analyses), as well as the environmental influences on lightning production in moist convection that vary substantially across regions (Boccippio et al. 2000; Gilmore and Wicker 2002). Finally, while most IFs may be predictive out to 30 min, we cannot conclude here how they compare regionally. The regional IF characteristics are compared in a follow-up study.

REFERENCES

Adler, R. F., and D. D. Fenn, 1979: Thunderstorm intensity as determined from satellite data. *J. Appl. Meteor.,* **18,** 502–517.

——, and R. A. Mack, 1986: Thunderstorm cloud top dynamics as inferred from satellite observations and a cloud top parcel model. *J. Atmos. Sci.,* **43,** 1945–1960.

Bergeron, T., 1935: On the physics of clouds and precipitation. *Proc. Fifth Assembly U.G.G.I.,* Lisbon, Portugal, International Union of Geodesy and Geophysics, 156–178.

Boccippio, D. J., S. J. Goodman, and S. Heckman, 2000: Regional differences in tropical lightning distributions. *J. Appl. Meteor.,* **39,** 2231–2248.

Cecil, D. J., S. J. Goodman, D. J. Boccippio, E. J. Zipser, and S. W. Nesbitt, 2005: Three years of TRMM precipitation features. Part I: Radar, radiometric, and lightning characteristics. *Mon. Wea. Rev.,* **133,** 543–566.

CIMSS/SSEC, cited 2010: ASPB and CIMSS calibration projects and research. [Available online at http://cimss.ssec.wisc.edu/goes/calibration/.]

Curran, E. B., R. L. Holle, and R. E. López, 2000: Lightning casualties and damages in the United States from 1959 to 1994. *J. Climate,* **13,** 3448–3464.

Dye, J. E., C. A. Knight, V. Toutenhoofd, and T. W. Cannon, 1974: The mechanism of precipitation formation in northeastern Colorado cumulus III. Coordinated microphysical and radar observations and summary. *J. Atmos. Sci.,* **31,** 2152–2159.

——, W. P. Winn, J. J. Jones, and D. W. Breed, 1989: The electrification of New Mexico thunderstorms. Part I: The relationship between precipitation development and the onset of electrification. *J. Geophys. Res.,* **94,** 8643–8656.

Gilmore, M. S., and L. J. Wicker, 2002: Influences of the local environment on supercell cloud-to-ground lightning, radar characteristics, and severe weather on 2 June 1995. *Mon. Wea. Rev.,* **130,** 2349–2372.

Goodman, S. J., D. E. Buechler, and P. J. Meyer, 1988: Convective tendency images derived from a combination of lightning and satellite data. *Wea. Forecasting,* **3,** 173–188.

——, and Coauthors, 2005: The North Alabama Lightning Mapping Array: Recent severe storm observations and future prospects. *Atmos. Res.,* **76,** 423–437.

Gremillion, M. S., and R. E. Orville, 1999: Thunderstorm characteristics of cloud-to-ground lightning at the Kennedy Space Center, Florida: A study of lightning initiation signatures as indicated by the WSR-88D. *Wea. Forecasting,* **14,** 640–649.

Hondl, K. D., and M. D. Eilts, 1994: Doppler radar signatures of developing thunderstorms and their potential to indicate the onset of cloud-to-ground lightning. *Mon. Wea. Rev.,* **122,** 1818–1836.

Houghton, H. G., 1950: A preliminary quantitative analysis of precipitation mechanisms. *J. Meteor.,* **7,** 363–369.

Keighton, S. J., H. B. Bluestein, and D. R. MacGorman, 1991: The evolution of a severe mesoscale convective system: Cloud-to-ground lightning location and storm structure. *Mon. Wea. Rev.,* **119,** 1533–1556.

Kidder, S. Q., and T. H. Vonder Haar, 1995: *Satellite Meteorology: An Introduction.* Academic Press, 466 pp.

Koshak, W. J., and Coauthors, 2004: North Alabama lightning mapping array (LMA): VHF source retrieval algorithm and error analyses. *J. Atmos. Oceanic Technol.,* **21,** 543–558.

Krehbiel, P. R., 1986: The electrical structure of thunderstorms. *The Earth's Electrical Environment,* E. P. Krider and R. G. Roble, Eds., National Academy Press, 90–113.

——, R. J. Thomas, W. Rison, T. Hamlin, J. Harlin, and M. Davis, 2000: GPS-based mapping system reveals lightning inside storms. *Eos, Trans. Amer. Geophys. Union,* **81,** 21–25.

——, and Coauthors, 2006: The Washington DC metro area lightning mapping array. *Eos, Trans. Amer. Geophys. Union,* **87** (Fall Meeting Suppl.), Abstract AE33A-1053.

Lindsey, D. T., D. W. Hillger, L. Grasso, J. A. Knaff, and J. F. Dostalek, 2006: GOES climatology and analysis of thunderstorms with enhanced 3.9-μm reflectivity. *Mon. Wea. Rev.,* **134,** 2342–2353.

MacGorman, D. R., and Coauthors, 2008: TELEX: The Thunderstorm Electrification and Lightning Experiment. *Bull. Amer. Meteor. Soc.,* **89,** 997–1013.

Mazany, R. A., S. Businger, S. I. Gutman, and W. Roeder, 2002: A lightning prediction index that utilizes GPS integrated precipitable water vapor. *Wea. Forecasting,* **17,** 1034–1047.

McCaul, E. W., Jr., S. J. Goodman, K. M. LaCasse, and D. J. Cecil, 2009: Forecasting lightning threat using cloud-resolving model simulations. *Wea. Forecasting,* **24,** 709–729.

McNamara, T. M., 2002: The horizontal extent of cloud-to-ground lightning over the Kennedy Space Center. M.S. thesis, Dept. of Engineering Physics, Air Force Institute of Technology, 114 pp.

McNish, L., cited 2010: RASC Calgary Centre—Latitude and longitude. [Available online at http://www.calgary.rasc.ca/latlong.htm.]

Mecikalski, J. R., and K. M. Bedka, 2006: Forecasting convective initiation by monitoring the evolution of moving cumulus in daytime GOES imagery. *Mon. Wea. Rev.,* **134,** 49–78.

——, S. J. Paech, K. M. Bedka, and L. A. Litten, 2008: A statistical evaluation of GOES cloud-top properties for nowcasting convective initiation. *Mon. Wea. Rev.,* **136,** 4899–4914.

——, W. M. Mackenzie Jr., M. Koenig, and S. Muller, 2010a: Cloud-top properties of growing cumulus prior to convective initiation as measured by Meteosat Second Generation. Part I: Infrared fields. *J. Appl. Meteor. Climatol.,* **49,** 521–534.

——, ——, ——, and ——, 2010b: Cloud-top properties of growing cumulus prior to convective initiation as measured by Meteosat Second Generation. Part II: Use of visible reflectance. *J. Appl. Meteor. Climatol.,* **49,** 2544–2558.

Menzel, W. P., and J. F. Purdom, 1994: Introducing GOES-I: The first of a new generation of geostationary operational environmental satellites. *Bull. Amer. Meteor. Soc.,* **75,** 757–781.

Mueller, C., T. Saxen, R. Roberts, J. Wilson, T. Betancourt, S. Dettling, N. Oien, and J. Yee, 2003: NCAR Auto-Nowcast System. *Wea. Forecasting,* **18,** 545–561.

Murphy, M. J., K. L. Cummins, N. W. S. Demetriades, and W. P. Roeder, 2008: Performance of the new Four-Dimensional Lightning Surveillance System (4DLSS) at the Kennedy Space Center/Cape Canaveral Air Force Station complex. *Extended Abstracts, 13th Conf. on Aviation, Range and Aerospace Meteorology,* New Orleans, LA, Amer. Meteor. Soc., 8.6. [Available online at http://ams.confex.com/ams/88Annual/techprogram/paper_131130.htm.]

NASA, cited 2010: FTP index. [Available online at ftp://trmm.ksc.nasa.gov/lightning/archives/4DLSS.]

National Weather Service, cited 2010: Natural hazard statistics. [Available online at http://www.nws.noaa.gov/om/hazstats.shtml.]

Nelson, L. A., 2002: Synthesis of 3-dimensional lightning data and weather radar data to determine the distance that naturally occurring lightning travels from thunderstorms. M.S. thesis, Dept. of Engineering Physics, Air Force Institute of Technology, 85 pp.

Orville, R. E., 1991: Lightning ground flash density in the contiguous United States—1989. *Mon. Wea. Rev.,* **119,** 573–577.

——, and G. R. Huffines, 2001: Cloud-to-ground lightning in the United States: NLDN results in the first decade, 1989–98. *Mon. Wea. Rev.,* **129,** 1179–1193.

Reynolds, S. E., M. Brook, and M. F. Gourley, 1957: Thunderstorm charge separation. *J. Atmos. Sci.,* **14,** 426–436.

Rison, W., S. Miller, and S. Hunyday, 2003: New Mexico Tech Lightning Mapping Array: Real-time system monitoring and data display. *Eos, Trans. Amer. Geophys. Union,* **84** (Fall Meeting Suppl.), Abstract AE22A-1108.

Roberts, R. D., and S. Rutledge, 2003: Nowcasting storm initiation and growth using GOES-8 and WSR-88D data. *Wea. Forecasting,* **18,** 562–584.

Roohr, P. B., and T. H. Vonder Haar, 1994: A comparative analysis of the temporal variability of lightning observation and GOES imagery. *J. Appl. Meteor.,* **33,** 1271–1290.

Rosenfeld, D., W. L. Woodley, A. Lerner, G. Kelman, and D. T. Lindsey, 2008: Satellite detection of severe convective storms by their retrieved vertical profiles of cloud particle effective radius and thermodynamic phase. *J. Geophys. Res.,* **113,** D04208, doi:10.1029/2007JD008600.

Saunders, C. P. R., 1993: A review of thunderstorm electrification processes. *J. Appl. Meteor.,* **32,** 642–655.

Setvák, M., and C. A. Doswell III, 1991: The AVHRR channel 3 cloud top reflectivity of convective storms. *Mon. Wea. Rev.,* **119,** 841–847.

Short, D. A., J. E. Sardonia, W. C. Lambert, and M. M. Wheeler, 2004: Nowcasting thunderstorm anvil clouds over Kennedy Space Center and Cape Canaveral Air Force Station. *Wea. Forecasting,* **19,** 706–713.

Siewert, C., 2008: Nowcasting lightning initiation through the use of infrared observations from the GOES satellite. M.S. thesis,

Atmospheric Science Dept., University of Alabama in Huntsville, 105 pp.

——, M. Koenig, and J. R. Mecikalski, 2010: Application of Meteosat Second Generation data towards improving the nowcasting of convective initiation. *Meteor. Appl.,* in press.

Thomas, R. J., P. R. Krehbiel, W. Rison, T. Hamlin, J. Harlin, and D. Shown, 2001: Observations of VHF source powers radiated by lightning. *Geophys. Res. Lett.,* **28,** 143–146.

——, ——, ——, S. J. Hunyady, W. P. Winn, T. Hamlin, and J. Harlin, 2004: Accuracy of the Lightning Mapping Array. *J. Geophys. Res.,* **109,** D14207, doi:10.1029/2004JD004549.

Wilks, D. S., 2006: *Statistical Methods in the Atmospheric Sciences.* 2nd ed. Academic Press, 627 pp.

Williams, E. R., 1988: The electrification of thunderstorms. *Sci. Amer.,* **259,** 48–65.

——, and R. E. Orville, 1989: The relationship between lightning type and convective state of thunderclouds. *J. Geophys. Res.,* **94,** 13 213–13 220.

——, V. Mushtak, D. Rosenfeld, S. Goodman, and D. Boccippio, 2005: Thermodynamic conditions favorable to superlative thunderstorm updraft, mixed phase microphysics and lightning flash rate. *Atmos. Res.,* **76,** 288–306.